Three-invariant model and bifurcation analysis of deformation bands for a sandstone subjected to true triaxial loading paths

Cyrille Couture, Pierre Bésuelle

Metadata of the article that will be visualized in OnlineFirst

ArticleTitle	Three-invariant model and bifurcation analysis of deformation bands for a sandstone subjected to true triaxial loading paths
Article Sub-Title	
Article CopyRight	
Journal Name	Acta Geotechnica
Corresponding Author	FamilyName **Couture** Particle Given Name **Cyrille** Suffix Division CNRS, Grenoble INP, 3SR Organization Université Grenoble Alpes Address 38000, Grenoble, France Phone Fax Email cyrille.couture@3sr-grenoble.fr URL ORCID http://orcid.org/0000-0001-9073-3926
Author	FamilyName **Bésuelle** Particle Given Name **Pierre** Suffix Division CNRS, Grenoble INP, 3SR Organization Université Grenoble Alpes Address 38000, Grenoble, France Phone Fax Email pierre.besuelle@3sr-grenoble.fr URL ORCID
Schedule	Received 25 Sep 2022 Revised Accepted 24 Jan 2023
Abstract	This paper presents a general three-invariant model to evaluate the theoretical prediction of strain localization against laboratory measurements performed during mechanical loading experiments, for a high-porosity Vosges sandstone (North-Eastern France). The model is based on a mean stress and Lode angle-dependent yield surface, calibrated using extensive experimental data from mechanical tests in triaxial, biaxial and true triaxial loading conditions. The general expression of a three-invariant and non-associated constitutive relation is then developed for 10 true triaxial loading paths, performed at constant mean stresses and prescribed Lode angles. The Rice's criterion by bifurcation analysis enables the theoretical prediction of deformation bands (onset, orientation and volumetric strain). The qualitative evolution of predicted band kinematics, as well as quantitative values obtained for the 10 loading paths, proves to be in good agreement with experimental observations from full-field characterization of localized zones. The relevance and predictiveness of the presented three-invariant model are further evidence by comparisons with simplified, associated and two-invariant models using the same initial dataset.
Keywords (separated by '-')	Bifurcation - Constitutive modeling - Deformation band - Experimental mechanics - Localization - Sandstone - Shear band - Stress invariants - True triaxial - Yield surface
Footnote Information	

Acta Geotechnica
https://doi.org/10.1007/s11440-023-01811-w

RESEARCH PAPER

Three-invariant model and bifurcation analysis of deformation bands for a sandstone subjected to true triaxial loading paths

Cyrille Couture[1] · Pierre Bésuelle[1]

Received: 25 September 2022 / Accepted: 24 January 2023

Abstract
This paper presents a general three-invariant model to evaluate the theoretical prediction of strain localization against laboratory measurements performed during mechanical loading experiments, for a high-porosity Vosges sandstone (North-Eastern France). The model is based on a mean stress and Lode angle-dependent yield surface, calibrated using extensive experimental data from mechanical tests in triaxial, biaxial and true triaxial loading conditions. The general expression of a three-invariant and non-associated constitutive relation is then developed for 10 true triaxial loading paths, performed at constant mean stresses and prescribed Lode angles. The Rice's criterion by bifurcation analysis enables the theoretical prediction of deformation bands (onset, orientation and volumetric strain). The qualitative evolution of predicted band kinematics, as well as quantitative values obtained for the 10 loading paths, proves to be in good agreement with experimental observations from full-field characterization of localized zones. The relevance and predictiveness of the presented three-invariant model are further evidence by comparisons with simplified, associated and two-invariant models using the same initial dataset.

Keywords Bifurcation · Constitutive modeling · Deformation band · Experimental mechanics · Localization · Sandstone · Shear band · Stress invariants · True triaxial · Yield surface

1 Introduction

Deformation processes in mechanically stressed geomaterials often lead to the development of planar kinematic zones of highly localized strain at failure, known as deformation or shear bands. The occurrence of this pervasive structural mode of deformation has been widely observed both in the field [2, 15, 20] and in laboratory settings [7, 10, 47, 53, 59].

In cohesive granular material such as porous sandstone, well-developed mature deformation bands are often indicative of a degenerative failure mode, resulting in a non-reversible transition in the global mechanical response near and beyond the peak stress. The emergence of these localized structures is generally concurrent with the culmination of a global weakening of the material through the accumulation of inelastic deformations, leading to a transition into the softening and permanent regimes. A theoretical study of these modes of localized deformation, in relation to rarely studied true triaxial stress states representative of underground rock formations, is of clear interest to better understand and predict mechanical conditions leading to transition failure modes of confined porous rocks.

The study of material bifurcation aims to evaluate the existence of constitutive limit states in the material, for which, in addition to further homogeneous deformation, a non-uniform kinematic solution is admissible. In particular, localized bifurcation modes, as opposed to diffuse bifurcation (*e.g.*, bulging and buckling modes), are highly relevant to the field of geomechanics, since they can be related to the emergence of material instabilities and abrupt transitions in deformation mechanisms. This type of analysis helps to further investigate geometrical aspects of kinematic structures at failure and therefore provides

✉ Cyrille Couture
cyrille.couture@3sr-grenoble.fr

Pierre Bésuelle
pierre.besuelle@3sr-grenoble.fr

[1] CNRS, Grenoble INP, 3SR, Université Grenoble Alpes, 38000 Grenoble, France

Journal : Large 11440 | Dispatch : 10-2-2023 | Pages : 14
Article No. : 1811 | ☐ LE | ☐ TYPESET
MS Code : AGEO-D-22-01165R1 | ☑ CP | ☑ DISK

valuable predictions of dominant deformation modes controlling the mechanical response during the post-peak regime.

A particular case of localized bifurcation can be studied within the Thomas–Hill–Mandel deformation band model [25, 37, 56]. This formalism provides a set of theoretical conditions for the emergence of deformation bands in the material continuum. The deformation band is therefore conceptualized as a material layer of infinite length in a plane and of finite thickness, bounded by two parallel surfaces, characterized by a weak discontinuity in the incremental displacement gradient [25]. This form of an idealized deformation band considers the compatibility of one or multiple planar localized zone with an equilibrium constitutive bifurcation state in the material and a set of prescribed boundary conditions at the interface [5, 50, 58].

To the authors' knowledge, few scientific works have systematically examined and compared with experiments the effect of true triaxial conditions on the prediction of deformation localization (*e.g.*, [11, 17, 23, 27, 43]). This is probably due to the scarcity of such experimental data, especially for porous rocks, where laboratory-scale experimental tests are generally carried out on axisymmetric loading paths, very often in compression (*e.g.*, [48]), sometimes in extension [6, 24], or more rarely in plane stress [38] and plane strain compression [29, 32, 46]. In a limited number of studies, experiments have also been performed under true triaxial conditions, allowing the effect of the intermediate principal stress or Lode angle to be fully studied [1, 13, 19, 22, 26, 35, 40, 42, 52, 55].

The effect of the Lode angle on the theoretical localization conditions is twofold. On the one hand, the anisotropy of the stress tensor is sufficient to induce a dependence with the Lode angle. On the other hand, the constitutive law can itself include a dependence on the Lode angle, which adds an effect on the localization conditions. This dependence of the constitutive law can be introduced by a non-circular shape of the yield or limit surfaces, as well as the plastic potential, in the octahedral (deviatoric) plane. Examples of such surfaces can be found in the literature, such as the Mohr–Coulomb surface or other smooth surfaces [8, 31, 39, 57, 60].

In the scope of the present study, the bifurcation analysis follows on the seminal development for geomaterials proposed in [51]. For this type of material, the constitutive behavior is expressed using a non-associated, pressure-dependent elasto-plastic relation. The specific model presented in this paper is extended to a three-invariant-dependent high-porosity sandstone from the Vosges region in France. The analysis considers the constitutive state of this material at the peak stress, where the initiation conditions for the emergence of fully developed deformation bands are met in the brittle and brittle–ductile transition regimes of the studied sandstone.

Using experimental data for the Vosges sandstone reported in [13], the deformation bands kinematics, their orientation and dilatancy angle, are theoretically predicted for different loading paths. The model parameters, *i.e.,* the normal to the yield surface, the direction of plastic strain and the elastic moduli, are first retrieved from the macroscopic response of the material. The deformation band kinematics at the peak stress predicted from the bifurcation analysis using this model are then compared to full-field experimental measurements, as well as alternative and simplified models using the same dataset.

Hereafter, the index summation convention is used and δ_{ij} is the Kronecker delta.

2 Constitutive model

This section describes a constitutive model, with isotropic and no time dependence assumptions, which is used for the later presented bifurcation analysis. The model is inspired by several series of experimental test results on a Vosges sandstone, including tests under true triaxial conditions. For the present analysis, the constitutive model is based on a classical development in elasto-plasticity with an additive decomposition of the total strain rate, $d\epsilon_{ij} = d\epsilon^e_{ij} + d\epsilon^p_{ij}$, where $d\epsilon^e$ and $d\epsilon^p$ denote the elastic and plastic strain rates, respectively. The constitutive tensor, defining the relation between incremental stress and strain ($d\sigma_{ij} = L_{ijkl}\, d\epsilon_{kl}$), is established according to the development of an isotropic work-hardening material. It can therefore be expressed as

$$L_{ijkl} = E_{ijkl} - \frac{1}{h} E_{ijuv} P_{uv} Q_{mn} E_{mnkl} \ , \tag{1}$$

with $h = H + Q_{ij} E_{ijkl} P_{kl}$ where H is a plastic coefficient, $\mathbf{E}$ is the elastic stiffness tensor, $\mathbf{Q}$ is the unit normal to the yield surface F and $\mathbf{P}$ is the direction of plastic strain increment, theoretically defined as the unit normal to a plastic potential surface G. The classical development of the constitutive relation is briefly presented in Appendix 1 for completeness. The yield surface F is described hereafter, based on experimental observations.

2.1 Yield surface description

In the current model, the three invariants of the stress tensor are introduced in the formulation of the yield surface. Compressive stresses are considered positive. The octahedral-Lode invariants are selected as a reference frame in a cylindrical coordinate system with the three invariants as

Journal : Large 11440 | Dispatch : 10-2-2023 | Pages : 14
Article No. : 1811 | LE | TYPESET
MS Code : AGEO-D-22-01165R1 | CP | DISK

$$
\begin{aligned}
\sigma_m &= \frac{1}{3} I_1 = \frac{1}{3}[\sigma_1 + \sigma_2 + \sigma_3] \ , \\
\tau_{oct} &= \sqrt{\frac{2}{3} J_2} \\
&= \frac{1}{3}\left[(\sigma_1 - \sigma_2)^2 + (\sigma_1 - \sigma_3)^2 + (\sigma_2 - \sigma_3)^2\right]^{1/2} \ , \\
\theta_\sigma &= \frac{1}{3} \arccos\left[\frac{3\sqrt{3}}{2}\frac{J_3}{J_2^{\frac{3}{2}}}\right] \\
&= \arctan\left[\sqrt{3}\frac{\sigma_2 - \sigma_3}{(\sigma_1 - \sigma_2) + (\sigma_1 - \sigma_3)}\right] \ ,
\end{aligned} \tag{2}
$$

where I and J are, respectively, the principal invariants of the second-order stress tensor and the deviatoric part of its additive decomposition, and σ_I are the three principal stresses (eigenvalues of the stress tensor). For consistency with loading paths from experiments considered in the calibration of the model, a single sextant of the octahedral plane is considered, where σ_1 and σ_3 are defined as the major (most compressive) and minor principal stresses, respectively. In this sector of the octahedral plane, and for the selected invariants in Eq. (2), $\theta_\sigma = 0^o$ and $\theta_\sigma = 60^o$ correspond, respectively, to an axisymmetric compression and axisymmetric extension stress state. An extrapolation of the model to the other five sectors of the octahedral plane is possible and requires the assumption that the studied rock is mechanically isotropic.

A suitable function for the yield surface of the modeled sandstone, with a dependency on the three invariants of the stress tensor, is selected based on restrictions on the convexity of the elastic domain and the continuity of its derivatives in the compressive stress regime. To this effect, a single continuous yield surface is deemed compatible with the observations of a progressive evolution in the deformation modes with both the mean stress and Lode angle. From a microstructural point of view, it implies that the change in deformation mechanisms from a brittle to a ductile regime, known to occur around the stationary point of the yield surface in the $\sigma_m - \tau_{oct}$ plane, is characterized by a smooth transition. Thus, the single yield surface for the present model is developed from a combination of two complementary functions, acting in both the $\sigma_m - \tau_{oct}$ (meridian) plane and the $\theta - \tau_{oct}$ (octahedral) plane in the compressive section of the stress space.

The first function is a mean stress-dependent linear–exponential (Linex) function

$$
F^a(\sigma_m) = A[e^{a_1(\sigma_m - a_2)} - a_1(\sigma_m - a_2) - a_3] \ , \tag{3}
$$

where a_i are fitting parameters influencing the shape (a_1) and the position (a_2 and a_3) of the function, and A is a scaling parameter. The single shape parameter, a_1, controls the steepness and asymmetry of the curve around the stationary point, where τ_{oct} reaches a maximum value. At limit values of the mean stress, the Linex function is dominated either by its linear term, at $a_1\sigma_m \rightarrow -\infty$, or by its exponential term, at $a_1\sigma_m \rightarrow +\infty$. Around the stationary point, the exponential and linear terms are of the same order of magnitude, resulting in a smooth transition in the curve. The choice of a Linex function is particularly well suited due to the ease of its differentiation, its convexity and the control it provides over the asymmetry of the curve, providing a good fit for experimental data in both the brittle and ductile regimes.

The second function is based on the van Eekelen [57] surface which is a relatively flexible function that can be adapted to various Lode angle-dependent forms and for which the friction angles in axisymmetric stress states ($\theta_\sigma = 0^o$ and 60^o) can be expressed independently. It is written as

$$
F^b(\theta) = B(1 - \xi \sin 3\theta)^n \ , \tag{4}
$$

where ξ and n are both shape parameters, and B is a scaling parameter. These parameters are bounded in a specific range to ensure the convexity of the fitted function. [57] has shown that a value for the exponent $n = -0.229$ provides an optimal range for the parameterization of ξ, over which the function remains convex. Selecting this value for n, the convexity limit of the function is $|\xi| \leq 0.793$ (In [57] β is used instead of ξ for the same parameter). A constant value of ξ implies a constant shape of the surface in all octahedral planes. Experimental observations on the distribution of peak stresses for mechanical experiments on porous rocks, including the Vosges sandstone studied here, have demonstrated a clear evolution of the shape with the mean stress. Consequently, a function taking into account this dependency should be evaluated according to the modeled material. Accordingly, a second-order polynomial,

$$
\xi(\sigma_m) = b_1 + b_2\sigma_m^2 \ , \tag{5}
$$

is selected to take into account this mean stress dependency. The upward open-endedness of the function guaranties the convexity limit is respected over the range of mean stresses. The suitability of the function to represent the shape parameter evolution is contingent on the experimental data and alternative functions for (5) can be selected without any difficulty.

Combining Eqs. (3), (4) and (5), the three-invariant yield surface in the Octahedral-Lode space can be formally written as

Journal : Large 11440 | Dispatch : 10-2-2023 | Pages : 14
Article No. : 1811 | LE | TYPESET
MS Code : AGEO-D-22-01165R1 | CP | DISK

$$F = \tau_{oct} - C\left\{e^{a_1(\sigma_m - a_2)} - a_1(\sigma_m - a_2) - a_3\right\}\left\{1 - (b_1 + b_2\sigma_m^2)\sin(3\theta)\right\}^n , \tag{6}$$

where C is a general scaling parameter. The outward normal to the yield surface, $\mathbf{Q}$, is simply defined in terms of the derivative of the yield surface with respect to the stress invariants and the Cauchy stress tensor using the flow rule. It can be written as

$$Q_{ij} = \frac{\partial F}{\partial \sigma_{ij}} = F_\sigma \frac{\partial \sigma_m}{\partial \sigma_{ij}} + F_\tau \frac{\partial \tau_{oct}}{\partial \sigma_{ij}} + F_\theta \frac{\partial \theta}{\partial \sigma_{ij}} , \tag{7}$$

where the subscript in F denotes the direction of the partial derivative with respect to each of the three octahedral-Lode invariants. The expansion of each derivative, while straightforward, can be quite extensive and is therefore provided in full in Appendix 2.

2.2 Yield surface calibration

The objective of this study is to determine the conditions for the existence of a localized solution, in the spirit of a bifurcation analysis similar to [51]. For this purpose, a complete description of the model, including the strain hardening law, is not necessary. Only the description of the yield surface, the plastic strain rate directions and the elastic moduli are required. The assumption will be made that when the bifurcation criterion is about to be satisfied, the yield surface shape approximates the experimentally obtained failure envelope [4, 45], this envelope being defined by the octahedral stress peaks of the different tests. The set of parameters in Eq. (6) is defined using the experimental measurements available for the Vosges sandstone. The different datasets used for this purpose consist of mechanical tests performed over a wide range of loading paths in axisymmetric triaxial compression [6], plane strain compression [32] and true triaxial compression [13]. The sandstone samples used in these three experimental campaigns were extracted from the same homogeneous block and therefore have similar initial mechanical properties. Additionally, the samples were all tested at a comparable laboratory scale, and under similar quasi-static and monotonic loading conditions.

The suitability of the second-order polynomial function in Eq. (5), taking into account the mean stress dependence of the parameter ξ in the octahedral plane, is first evaluated using the series of true triaxial experiments in [13]. For these experiments, the stress peaks are constrained by the selected loading paths to remain in specific octahedral planes, corresponding to two constant mean stresses of 60 MPa and 90 MPa. In each plane, where experiments at five different Lode angles are performed, the van Eekelen part of the yield surface in Eq. (4) is fitted to a single value of ξ, where a least square regression results in $\xi = -0.587$ and $\xi = -0.430$, at 60 MPa and 90 MPa, respectively. This increase in the value ξ reflects a clear evolution in the shape of the van Eekelen surface with increasing mean stress, as shown by the two data points represented in Fig. 1. These values can be compared to the continuous curve in Fig. 1, representing the evolution of ξ for the selected second-order polynomial function with parameters b_1 and b_2. The value of these two parameters is obtained by regression of Eq. (6), concurrently to other parameters in Table 1, and for the full dataset in triaxial, biaxial and true triaxial loading. This comparison confirms that the choice of the function for ξ, defining the shape evolution in the octahedral plane, is compatible with the yield surface optimization with the complete dataset of available peak stress values for the studied Vosges sandstone. Note that in Fig. 1, ξ tends toward the convexity limit as the mean stress approaches zero. The choice of a second-order polynomial ensures that the function remains above this limit for positive mean stresses. However, another choice of function could be made depending on the experimental data and different shape evolution of the surface for other rocks.

The six parameters defining the yield surface (Eq. 6) are fitted to the peak stress from the three datasets using a least square optimization scheme. The optimized parameters for the represented surface are provided in Table 1. A graphical representation of the yield surface for this set of parameters, along with the peak stress values retrieved from the different datasets, is shown in Fig. 2 for isovalues

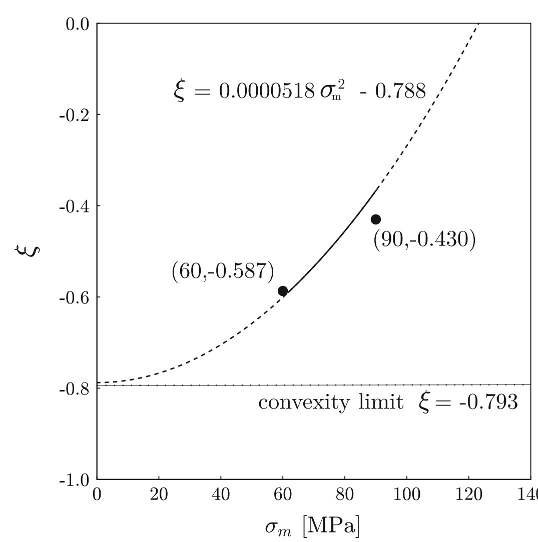

Fig. 1 Evolution of ξ with σ_m for a second-order polynomial function. The labeled points denote the value obtained from an independent regression at 60 MPa and 90 MPa using Eq. (4). The parameters b_1 and b_2 for the continuous curve are obtained from the least square regression on the combined formulation of the yield surface, in Eq. (6)

Journal : Large 11440 Dispatch : 10-2-2023 Pages : 14
Article No. : 1811 ☐ LE ☐ TYPESET
MS Code : AGEO-D-22-01165R1 ☑ CP ☑ DISK

Table 1 Yield surface parameters for the Vosges sandstone

Parameter	Value	Unit
n [1]	-0.229	1
C	-42.5	MPa
a_1	0.0185	MPa^{-1}
a_2	108	MPa
a_3	2.22	1
b_1	-0.788	1
b_2	5.18×10^{-5}	MPa^{-2}

[1] The parameter n is prescribed and not optimized in the fitted function

angle, as evidenced by the triangular shape of the yield surface in the octahedral plane. The mean stresses dependence of ξ influences the shape of the yield surface to evolve from an upward triangular shape, at low mean stress, toward a circular shape, at $\sigma_m = 123$ MPa corresponding to $\xi = 0$. Above this threshold, which occurs in the domain $F_\sigma < 0$, ξ becomes positive, showing a possibility for the deviatoric stress peaks at a high Lode angle to be higher than the peak at a low Lode angle. Evidently, this failure regime falls outside of the available data points for the studied set of experiments and the choices are rather arbitrary and could have been different. Nonetheless, the continuous evolution of the yield surface, for $\sigma_m > 123$ MPa, into a downward triangular shape, shown in Fig. 2c, has been observed in analog high-porosity sandstone and carbonate rocks [16, 36].

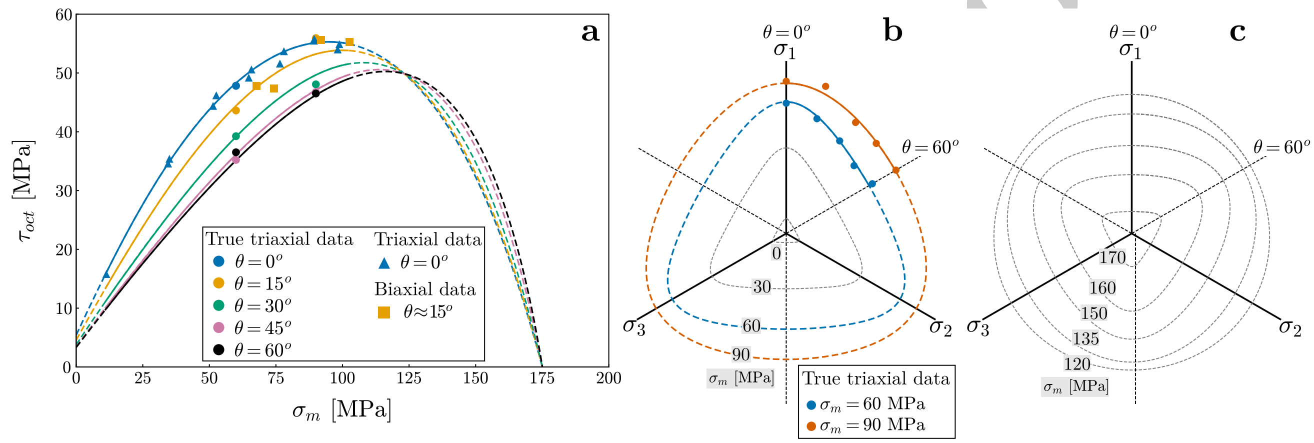

Fig. 2 Representation of the peak octahedral stresses for different stress paths from three experimental datasets on the studied Vosges sandstone. The curves represent the yield surface from Eq. (6) with fitted parameters from Table 1. The shape evolution of the yield surface is clearly visible for both isovalues of Lode angles in the meridian plane (**a**), and isovalues of mean stresses in the octahedral planes, for low σ_m in (**b**) and high σ_m in (**c**)

of θ, in the meridian planes, and isovalues of σ_m, in the octahedral planes. Note that both sets of isovalue curves are convex, which is a necessary condition for the convexity of the 3D surface.

In these cross-sectional plane representations, the complementarity of the different datasets to generate a well-defined yield surface in the 3D stress space is apparent. In the meridian plane, the shape of the yield surface is mostly influenced by experiments performed in triaxial axisymmetric compression ($\theta = 0^o$) for a large range of mean stresses up to the stationary point (*i.e.*, at the change in the sign of F_σ). Additionally, the true triaxial dataset, spanning the entire sextant of the octahedral plane at two mean stress levels, captures effectively the influence of the Lode angle. It is complemented by biaxial (plane strain) experiments, with peak stresses situated where the shape of the yield surface varies more significantly with respect to the Lode angle, around $\theta = 15^o$.

In the range of available peak stress data where $F_\sigma > 0$, the peak stress consistently decreases with increasing Lode

2.3 Elastic moduli from experiments

The elastic stiffness tensor $\mathbf{E}$ is evaluated from the stress–strain measurements during isotropic and deviatoric loading of true triaxial mechanical tests reported in [13]. Therefore, in this section and onward, the specific method is presented to determine the elastic moduli for the Vosges sandstone, in the context of loading paths with prescribed invariants of the stress tensor.

Under the assumption of isotropic linear elasticity, with applicable symmetries in the constitutive tensor, the elastic part of the stress–strain relation is

$$d\sigma_{ij} = 3K\left(\frac{1}{3}d\epsilon^e_{kk}\delta_{ij}\right) + 2S\left(d\epsilon^e_{ij} - \frac{1}{3}d\epsilon^e_{kk}\delta_{ij}\right) , \qquad (8)$$

with the elastic properties of the material determined by the

Journal : Large 11440 | Dispatch : 10-2-2023 | Pages : 14
Article No. : 1811 | LE | TYPESET
MS Code : AGEO-D-22-01165R1 | CP | DISK

bulk modulus (K) and shear modulus (S). For an initially isotropic loading phase, the deviatoric part of the elastic strain tensor theoretically vanishes, resulting in $d\sigma_{ij} = K d\epsilon^e_{kk}\delta_{ij}$. Similarly, during the subsequent purely deviatoric loading phase, at constant mean stress, the elastic part of the volumetric strain vanishes, resulting in $d\sigma_{ij} = 2Sd\epsilon^e_{ij}$. Consequently, the two elastic moduli can be retrieved individually from the isotropic and deviatoric loading phases as

$$K = \frac{\Delta\sigma_m}{\Delta\epsilon^e_v}\ , \text{ and } S = \frac{\Delta\tau_{oct}}{2\Delta\gamma^e_{oct}}\ , \tag{9}$$

in terms of the first and second invariants, respectively. The constitutive fourth-order elastic tensor can be expressed using the Lamé parameters, $\lambda = K - \frac{2}{3}S$, $\mu = S$, as

$$E_{ijkl} = \lambda\,\delta_{ij}\delta_{kl} + \mu\left(\delta_{ik}\delta_{jl} + \delta_{il}\delta_{jk}\right)\ . \tag{10}$$

In the scope of this analysis, elastic moduli are defined from the ten loading paths in the range of mean stresses from 60 MPa to 90 MPa. Therefore, K and S, and the related Lamé duals, are, respectively, estimated from (i) the linear range of the isotropic and volumetric stress–strain curve between 60 and 90 MPa, and (ii) the average initial slope of the octahedral stress–strain curve. These estimated values are reported in Table 2.

It should be noted that elastic parameters are known to evolve according to the loading history [54], and an average scalar representation does not fully take into account this evolution of the material behavior during loading. For the studied Vosges sandstone, inelastic volumetric deformation present from the beginning of the deviatoric loading phase of the experiments suggests that the initial slope of the stress–strain octahedral curve does not correspond to a purely elastic behavior. Nonetheless, isotropic loading–unloading tests on a similar porous sandstone, studied by [41], have shown a decrease in the inelastic part of the volumetric deformations with increasing mean stress, accounting for less than 20% of the total volumetric strain above $\sigma_m = 40$ MPa. The importance of elasticity in the model will be assessed through a sensitivity analysis of the elastic moduli, in comparison with the influence of the plastic parameters (the outward normal **Q** and plastic strain increment **P**) evaluated at the stress peak.

Table 2 Elastic moduli

Parameter	Value (GPa)
K	10
S, μ	6.0
λ	6.0

2.4 Incremental plastic strain from experiments

In the following calculation of the incremental plastic strain direction **P**, the octahedral-Lode invariants of the plastic strain tensor ϵ^p_{ij}, are analog to the invariants expressed for the stress tensor in Eq. (2). For a coaxial model, the direction of plastic strain increment can be represented in the stress space where it is normalized for a unit increment of stress. For a non-associated model, **P** is normally assumed as the derivative of a plastic potential G, as

$$P_{ij} = \frac{\partial G}{\partial\sigma_{ij}} = G_\sigma\frac{\partial\sigma_m}{\partial\sigma_{ij}} + G_\tau\frac{\partial\tau_{oct}}{\partial\sigma_{ij}} + G_\theta\frac{\partial\theta_\sigma}{\partial\sigma_{ij}}, \tag{11}$$

where the subscripts in G denote the derivatives in the direction of each octahedral-Lode invariant. However, in the present analysis the plastic strain increments are evaluated directly from experimental measurements close to the peak octahedral stress. Therefore, its derivation from a generating function is only theoretical and the plastic potential does not need to be explicitly evaluated.

From the imposed constraints on σ_m and θ during the deviatoric loading phase, the elastic part of the strain increment vanishes in the direction of those invariants (*i.e.*, $\epsilon^e_{vol} = 0$ and θ^e_ϵ). Therefore, the shear modulus is taken into account only in the direction of deformation increments following the octahedral direction (*i.e.*, the radial direction in the octahedral plane). The strain invariants $\epsilon_{vol}, \gamma_{oct}$ and θ_ϵ are therefore obtained from the principal strain measurements using a combination of strain gauges and averaged displacement from digital image correlation for the reported experiments in[13]. The incremental plastic strain are

$$\begin{aligned} G_\sigma &= \Delta(\epsilon_{vol} - \epsilon^e_{vol}) = \Delta\epsilon_{vol}\ , \\ G_\tau &= \Delta(\gamma_{oct} - \gamma^e_{oct}) = \Delta\gamma_{oct} - \frac{\Delta\tau_{oct}}{2S}\ , \\ G_\theta &= \Delta(\theta_\epsilon - \theta^e_\epsilon) = \Delta\theta_\epsilon\ , \end{aligned} \tag{12}$$

where S is the elastic shear modulus defined in Eq. (9). For all measurements, Δ represents a fixed time interval of 60 measurement points (at 1 Hz acquisition rate) before the peak octahedral stress. This time interval is selected in order to minimize errors in the measurement noise, acquisition synchronicity and stick-slip frictional behavior in the loading piston.

The orientations of the normalized **P** in the meridian and octahedral planes are represented in Fig. 3 for the ten true triaxial experiments. The origin of the arrows coincides with the yield surface, at the prescribed mean stress and Lode angle for each loading path, and where the normal **Q** is also represented. In the meridian plane representation, the orientation of **Q** is seen to be systematically lower than

Journal : Large 11440 | Dispatch : 10-2-2023 | Pages : 14
Article No. : 1811 | LE | TYPESET
MS Code : AGEO-D-22-01165R1 | CP | DISK

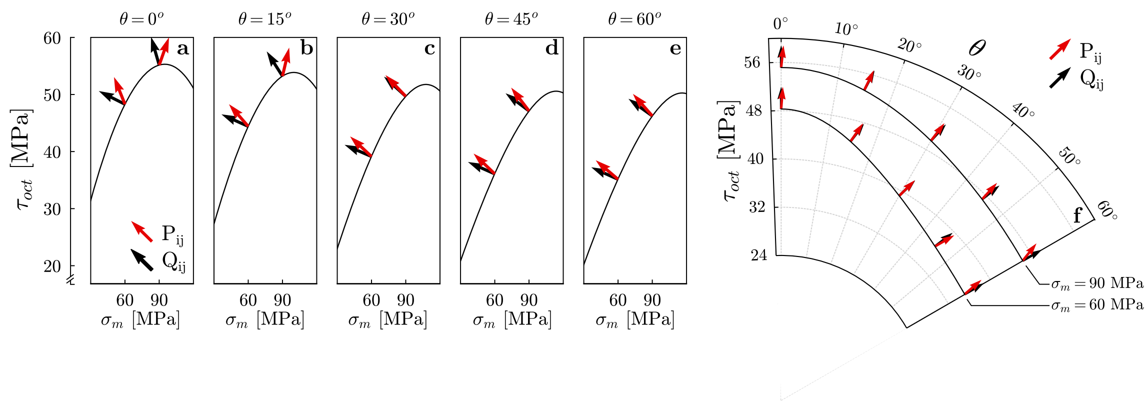

Fig. 3 Direction of the outward normal **Q** and plastic deformation direction, **P**, at the intersection of the yield surface and the respective loading paths in the meridian plane (**a**–**e**) and octahedral plane (**f**). In each plane, the orientations for each true triaxial experiment are represented at the two mean stresses of 60 MPa and 90 MPa, and the five Lode angles. In the meridian plane, non-associativity of the model is stronger at low Lode angles and weaker at high Lode angle. In the octahedral plane, deviatoric associativity is observed for all loading paths

P, where a significant difference in their orientation is most notable at lower Lode angles. This difference is less pronounced at Lode angles above 30^o, where fewer dissimilarities are observed between loading paths at both mean stresses. The orientation of both **P** and **Q** in the meridian planes tends to decrease as the Lode angle increases. The difference in the orientation of **P** and **Q** denotes a strong non-associativity for the Vosges sandstone in the meridian plane, *i.e.,* with respect to the effect of the mean stress. This type of non-associativity of the Vosges sandstone is consistent with reported observations from previous studies, which identified similar behavior in the meridian plane for high-porosity rocks [4, 28, 45]. Conversely, in the octahedral plane represented in Fig. 3f, **P** and **Q** are seen to have comparable outward orientations, suggesting a deviatoric associativity of the material. This characteristic of the model was also observed in non-cohesive geomaterials [30, 49, 61] and is often postulated in theoretical studies for the type of instabilities studied herein [34].

3 Bifurcation analysis

The following bifurcation analysis consists in seeking admissible localized kinematic solutions for the inception of strain localization. This bifurcation from initially homogeneous deformation is characterized by a loss of ellipticity in the material constitutive tensor, where multiple solutions to further deformation become possible. The material response is then contingent to the theoretical constraints on the nature of the localization structure, in the form of a planar deformation band of finite thickness. Based on the bifurcation framework proposed by [50], these constraints are imposed in the form of a kinematic condition, relating the rate of deformation inside and outside the deformation band, and an equilibrium condition, prescribing continuity in the traction rate at the band interfaces. As such, the surface boundaries of the localized region are defined by two parallel weak planar discontinuities, which orientation is described by the normal to the plane n, with a vanishing intermediate principal value [5]. The localization conditions appear to be strongly dependent on both the constitutive model and the nature of the loading.

Regarding the 3D planar orientation of the band, post-mortem X-ray scans of the sandstone samples revealed that the out-of-plane orientation of an average plane passing through the deformation band was generally well aligned with the intermediate principal stress direction [12]. Consequently, the initial assumption of a vanishing intermediate principal value of the deformation band can be confirmed and its orientation is represented only in the major–minor plane.

3.1 Deformation band angle prediction

From the set of prescribed conditions, a general criterion for continuous bifurcation is classically established as $det\left[L_{ijkl}n_jn_l\right] = 0$ [51]. For the model presented above, the constitutive tensor **L** is given by the elasto-plastic formulation expressed in Eq. (8). Solving the equation in terms of the plastic coefficient leads to

$$H = -\left(Q_{ij}E_{ijkl}P_{kl}\right) + \left(Q_{ij}E_{ijkl}n_l\right)\left(n_jn_lE_{ijkl}\right)^{-1}\left(n_jE_{ijkl}P_{kl}\right)\;. \tag{13}$$

From this expansion of the bifurcation criteria, with known material plastic and elastic parameters (**Q**, **P** and **E**) at the onset of strain localization, Eq. (13) relates the value of the plastic coefficient H to a direction of the deformation band unit normal n. The relation between H and β, the angle between n and the maximum principal stress direction in

Journal : Large 11440 Dispatch : 10-2-2023 Pages : 14
Article No. : 1811 LE TYPESET
MS Code : AGEO-D-22-01165R1 CP DISK

the localization plane, which satisfies the bifurcation criteria is shown in Fig. 4 for the 10 true triaxial loading paths. It is seen in this representation that a unique maximum for H can be identified for β in the range of 0° to 90°. The criteria for the angle of conjugated bands, at an angle symmetrical to the maximum principal stress axis, are also symmetrical. Conjugated band orientation duals are therefore associated with the same value of H and equally probable.

For a hardening solid, the tangent modulus of the constitutive relation continuously decreases during the accumulation of plastic strain. Therefore, [51] have argued that the critical orientation (n_c) for localization to occur is at the maximum, or critical, value of the plastic coefficient (H_c). It follows that the orientation n_c provides a prediction for the most likely band orientation in the minor-major principal plane. Figure 4 shows the maximum value of H/S to occur near the transition between the hardening and softening regime (stress peak) for $\theta > 0°$ and well in the softening regime for $\theta = 0°$.

Figure 5 shows the critical angle (β_c) predicted by the model for the different loading paths. It is seen to systematically increase with an increase in the Lode angle and a decrease in the mean stress. The change in angle is also more pronounced at lower Lode angles. These results can be compared to the deformation band angle measured experimentally at the peak octahedral stress, as reported in [13]. The model provides a good prediction of the general trend in the evolution of the band orientation, with increasing Lode angle. For most loading paths, the quantitative prediction of the deformation band angle is also in good agreement with observations. A discrepancy is noticeable for $\sigma_m = 90$ MPa and $\theta = 0^o$ and 15^o, where the deformation band angle is predicted at a lower angle than experimentally measured. This discrepancy can be attributed to the pronounced change in the normal to the yield surface in the meridian plane around $\sigma_m = 90$ MPa (see Fig. 2). With fewer data points available in this region of the plane, there is a higher uncertainty in the calibration of the yield surface.

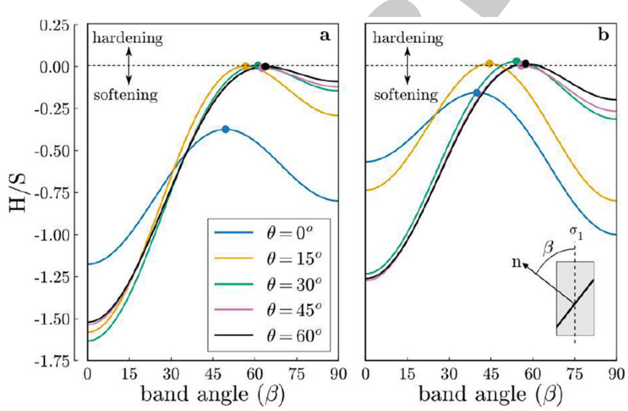

Fig. 4 Evolution of the normalized plastic coefficient (H/S) with respect to the deformation band angles satisfying the bifurcation criteria, for loading paths at 60 MPa (**a**) and 90 MPa (**b**) mean stress

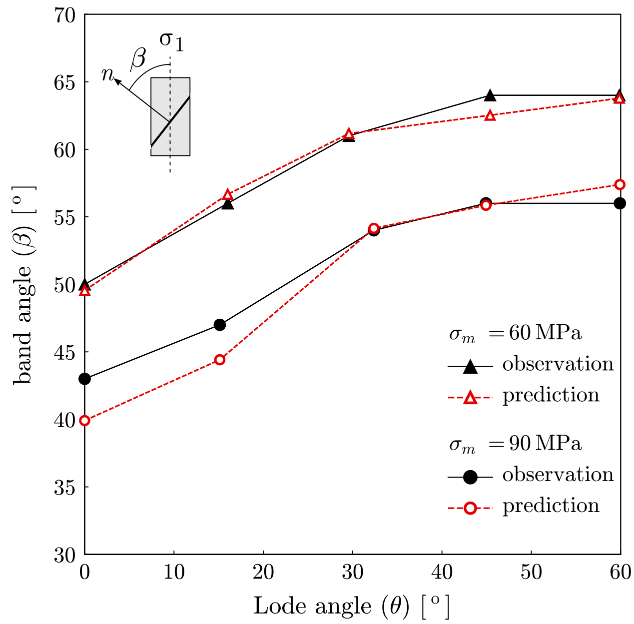

Fig. 5 Deformation band angle (β) with increasing Lode angle at the two mean stresses of 60 MPa and 90 MPa. The three-invariant model predictions are plotted against experimental observations

3.2 Dilatancy angle prediction

The dilatancy angle (ϕ) of the deformation band is defined, according to [4], as the ratio of volumetric and shear components of the deformation jump measured parallel to the band,

$$\tan\phi = \frac{\Delta D^{vol}}{\Delta D^{shear}} \ . \tag{14}$$

For the unit normal associated with the critical band angle, n^c,

$$\begin{aligned} \Delta D^{vol} &= g_s n_s^c \ , \\ \Delta D^{shear} &= \| \frac{1}{2}\left(g_k n_s^c + g_s n_k^c\right) n_k^c - D^{vol} n_s^c \| \end{aligned} \tag{15}$$

are the change in volumetric and shear deformation in the normal and tangential directions of the deformation band. The directional vector g is derived from the bifurcation condition as

$$g_k = \gamma\left(n_j^c n_l^c E_{ijkl}\right)^{-1}\left(n_j^c E_{ijmn} P_{mn}\right) \ , \tag{16}$$

where γ is an arbitrary constant multiplier.

For the two investigated mean stresses, the predicted dilatancy angle over the range of Lode angles is shown in

Journal : Large 11440 | Dispatch : 10-2-2023 | Pages : 14
Article No. : 1811 | LE | TYPESET
MS Code : AGEO-D-22-01165R1 | CP | DISK

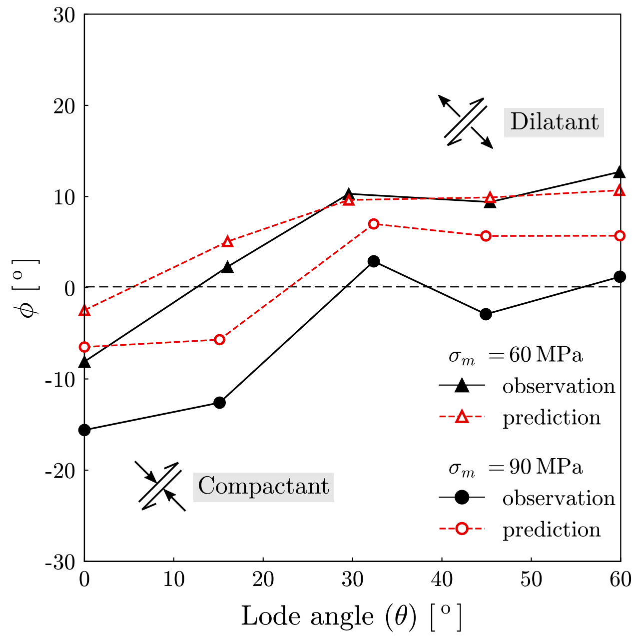

Fig. 6 Dilatancy angle (ϕ) across the deformation band with increasing Lode angle, at the two mean stresses of 60 MPa and 90 MPa. The three-invariant model predictions are plotted against experimental observations. A negative value of the angle denotes compaction and a positive value denotes a dilation associated to the shearing

Fig. 6. Similarly to the deformation band angle, the dilatancy angle can be compared to an experimental value at the peak stress. The experimental dilatancy angles were determined from respective displacement fields obtained by digital image correlation over strain increments where the deformation band is seen to emerge on the surface of the sample [13]. Since this value of the dilatancy angle is assessed from an average measurement of the propagating band, it is not constant over the length of the deformation band and is thus sensitive to some variability in the band inclination. Considering these uncertainties in the measurement of ϕ from the displacement field, the trend in the evolution of observed and predicted dilatancy angle is reasonably well matched. At the low mean stress of 60 MPa, where strain localization initially concentrates into narrow and straight mature deformation bands, experimental measurements of the band angles are also in good quantitative agreement with the model prediction. At the higher mean stress of 90 MPa, the predicted dilatancy angle is more dilatant than for experimental observations. Nonetheless, the evolution of the dilatancy angle with the Lode angle is generally well represented in the model, with the correct tendency for dilatancy or compaction associated to the shearing through the deformation band.

3.3 Alternative models and elastic sensitivity

The development of the constitutive model introduced above is made possible thanks to extensive experimental data available for the studied Vosges sandstone. The experimental methods to retrieve the model parameters further rely on an advanced true triaxial loading apparatus and sophisticated approaches to the acquisition of local strain measurements. Alternatively, most analyses in bifurcation reported in the literature are conducted using simplified models, for which some important mechanical behavior identified for porous rocks are not fully accounted for. It is the case for models dependent on two invariants of the stress tensor (Lode angle independent), and models assuming associated plasticity ($\mathbf{P} = \mathbf{Q}$). These model simplifications can be highly valuable, and sometimes necessary, when the shape of the yield surface in the octahedral plane cannot be defined, or when the directions of plastic strain at failure are not available or unreliable. In the same spirit as in the previous analysis, the deformation band kinematic can be predicted for these alternative models. In this section, their comparison with the initially presented model in terms of prediction accuracy enables us to assess the merit of added complexities in a more general approach.

The inclination of the deformation band and the band dilatancy angle are first predicted for a two-invariant model where the yield surface is optimized for the Linex function in the meridian plane, with a constant circular shape in the octahedral plane, *i.e.*, imposing $b_1 = b_2 = 0$ in Eq. (6). It results that the solution to the bifurcation criteria is not influenced by $F_\theta = 1$, but the effect of the Lode angle for the different stress paths is still accounted for in $\frac{\partial \theta}{\partial \boldsymbol{\sigma}}$. For this two-invariant model, the direction of plastic strain increment $\mathbf{P}$ remains unchanged compared to the initial three-invariant model.

The comparison of band angle, in Fig. 7a, shows that a two-invariant model leads to a systematic underestimation of β compared to the three-invariant model. This effect is most pronounced at higher Lode angles and lower mean stresses, where the outward normal to the van Eekelen surface in the initial model is most divergent from the radial direction. Concurrently, the predicted band dilatancy angle for this model, as seen in Fig. 7d, is higher than for the initial model, providing a less accurate prediction against experimental measurements.

A second predictive model comparison is made for an associated model, where directions of plastic strain rate would be a priori unknown and therefore assumed equal to the outward normal to the yield surface (*i.e.*, $\mathbf{P} = \mathbf{Q} = \frac{\partial F}{\partial \boldsymbol{\sigma}}$). Since the initial model is close to deviatoric associativity, the main effect of this simplified model lies in the imposed

Journal : Large 11440 | Dispatch : 10-2-2023 | Pages : 14
Article No. : 1811 | LE | TYPESET
MS Code : AGEO-D-22-01165R1 | CP | DISK

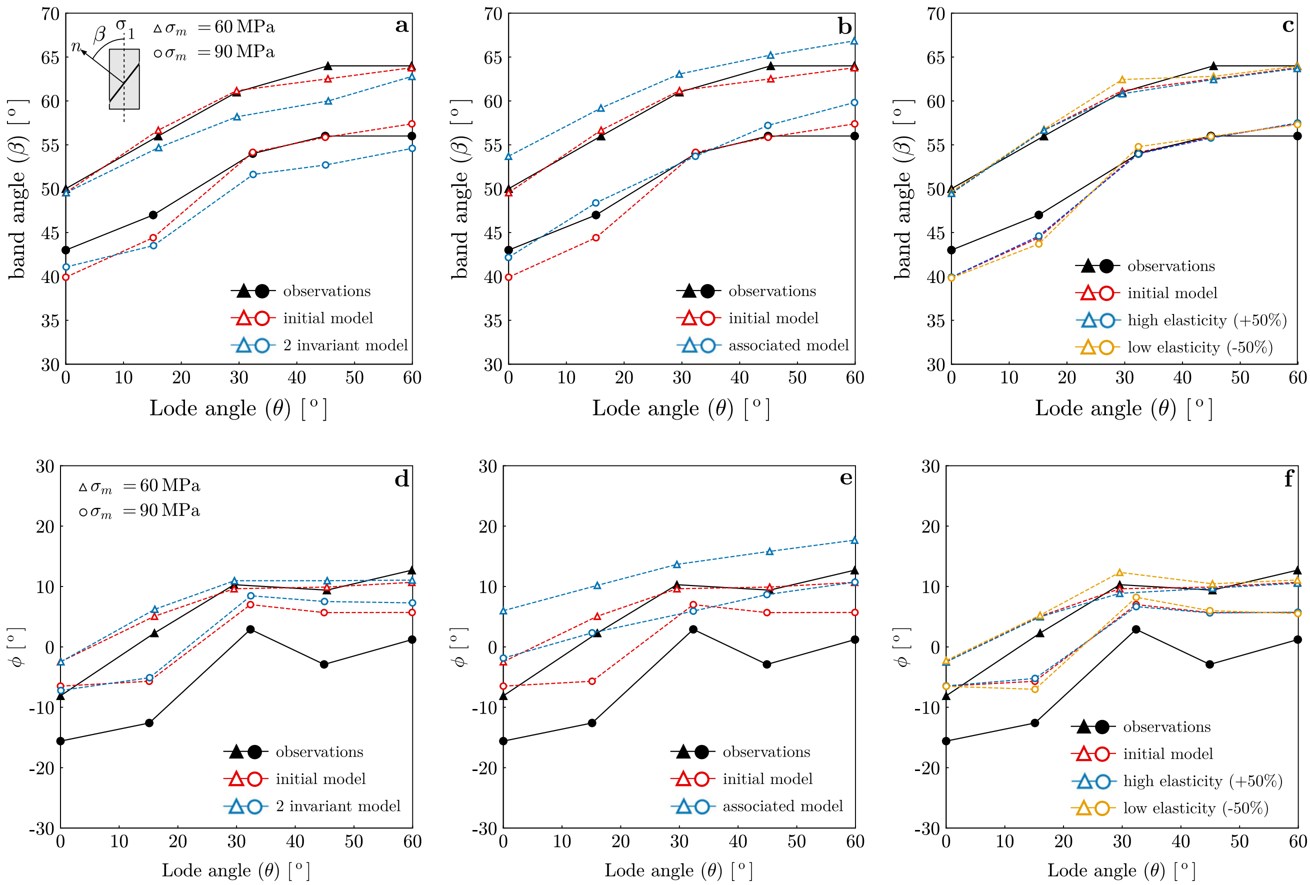

Fig. 7 Comparison of the deformation band angle (**a**, **b**, **c**) and band dilatancy angle prediction (**d**, **e**, **f**) between experimental observations (black), the initially presented three-invariant and non-associated model (red) and alternative models (blue, green): two-invariant model (**a**, **d**), associated model (**b**, **e**) and elastic moduli sensitivity (**c**, **f**)

associativity in the meridian plane. Therefore, imposing the direction of **P** for an intrinsically non-associated sandstone overestimates the dilatancy of the material and leads to an increase in both the deformation band angle (Fig. 7b) and band dilatancy angle (Fig. 7e) predicted by the bifurcation analysis. This results in a poorer prediction at 60 MPa, as well as for the high Lode angles at 90 MPa. At low Lode angle and a mean stress of 90 MPa, this model improves the prediction of the band angle β. However, this is due to a volume behavior that is considered to be dilating, whereas it is measured as contracting (Fig. 7e).

The sensitivity of the initial model to variations in the elastic parameters extracted from the stress–strain relations is evaluated by prescribing, in two different cases, a 50% increase and decrease in both the bulk and shear elastic moduli. Figure 7c and f shows that, even for such large variations in the elastic parameters, the predicted band angle and dilatancy angle remain mostly unaffected. These results demonstrate the marginal effect of possibly large uncertainties in the values for the elastic parameters selected in this analysis. The observation of such a small effect is consistent with the loading of a rock material since, under the present conditions, elastic strains remain small compared to plastic strains at the onset of bifurcation. In fact, higher moduli, or a stiffer elastic response, would not change the prediction. However, for lower elastic moduli of the material, in the order of the hardening modulus, the elastic contribution would have a significant influence on the deformation response and thus on the resulting kinematic predictions.

4 Discussion

Some considerations in the bifurcation criteria and constitutive relation considered previously are hereafter contextualized and compared to recent experimental observations, as well as known deformation mechanisms occurring in porous rocks.

In the previous section, the kinematics predictions from the bifurcation analysis were compared to laboratory experimental data for a porous sandstone, obtained by full-field measurements and digital image correlation [13]. The authors of the experimental study described different

Journal : Large 11440 | Dispatch : 10-2-2023 | Pages : 14
Article No. : 1811 | LE | TYPESET
MS Code : AGEO-D-22-01165R1 | CP | DISK

localized deformation modes and their evolution, from the beginning of the deviatoric loading phase to a post-peak state after substantial and well-developed strain localization.

The authors introduced a distinction between early deformation bands, appearing well before the stress peak, and mature deformation bands, emerging near the stress peak and initiating a softening response of the material. In the presented bifurcation analysis, as well as in previous studies where bifurcation theory is used to evaluate the localization behavior of rocks, it is the kinematics of mature deformation bands that are predicted by the theoretical results. Therefore, the presented analysis is based on a model for the constitutive state of the material at their inception, considering a diffuse deformation prior to the development of mature strain localization. However, if the onset of mature strain localization bands can be considered as a matter of non-uniqueness of solution, as introduced by bifurcation analysis, what about early localization bands?

In contrast to mature localization, the early localization regions are characterized by numerous parallel and conjugate bands, where shear deformation is concentrated. These bands also exhibit a dilatant behavior which induces a relative dilatancy at the sample scale. Similarly, they are concomitant with a loss of linearity in the octahedral stress *vs.* strain response. As the loading progresses, the number of active early bands decreases, and as the peak is approached, a localization zone associated with a loss of sample strength (initiation of softening) appears. The orientation of the early and mature bands is close but differs by a few degrees.

This mode of early localization has also been observed in a clayey rock under specific loading conditions (for sufficiently high mean stresses) [3]. One may also wonder whether the secondary localization bands in a carbonate rock observed *postmortem* by Mogi ([42], fig. 3.78) are not evidence of an early localization? Furthermore, early localization has also been observed in granular materials [18, 33].

On the numerical modeling side, a few studies have reported this pre-peak localization. In the context of modeling in a continuous medium, it is generally observed if a slight material heterogeneity has been introduced into the medium [21, 44]. It is also observed in the context of discrete medium modeling [14].

Thus, it appears that the localization process in sandstone occurs in two stages. A first early stage (before the peak stress) is characterized by a large number of short bands inducing a change in the tangential stiffness and dilatancy of the sample, without inducing a softening of the sample. It is followed by a second stage which sees the appearance of mature bands, which may be dilating or contracting depending on the level of mean stress and Lode angle, and induces a softening of the sample. Microstructural observations of early and mature shear bands have been done on the same Vosges sandstone loaded under plane strain compression [32]. The early bands appear to be marked by low damage (intragranular and intergranular cracking), while the mature bands are characterized by high damage (grain crushing).

This second phase of localization, inducing a strong microstructural change of the material, and in the loading conditions studied here, a softening of the material, is consistent with the predictions of the bifurcation analysis. Let us recall that the Rice's bifurcation criterion can be interpreted as a state linked to the existence of a direction n and a kinetic g for which the mechanical response in the band corresponds to the condition $(L_{ijkl}\, g_k\, n_l)\, n_j = \dot{\sigma}_{ij}\, n_j = 0$ due to the predominance of the in-band kinetic compared to the out-of-band kinetic (infinite ratio) [9]. In other words, considering the incipient band as a layer undergoing a homogeneous deformation over its thickness, described by $1/2\,(g_k\, n_l + g_l\, n_k)$, the traction vector rate applied to this layer is vanishing at the onset of localization. This kind of material response needs a substantial microstructural evolution that could be met only during the mature localization process. Clearly, further work will be needed to clarify the theoretical conditions for the early localization.

Another interesting aspect is the brittle–ductile transition in the mechanical behavior of porous rocks. This has been discussed in [13], in terms of the different views one can have on this transition, in terms of the pre-peak response, the post-peak response, the orientations of the localization bands, the volume strain within the bands and finally the more or less complex pattern of localization. A relevant prism to consider in this paper is the orientation of the bands and the nature of the deformation. It is now well understood that the orientation of the bands (angle between the band and the most compressive stress direction) increases during this transition and that also the volume strain associated with the shear deformation (slip parallel to the band) evolves from expansion to compaction, with the extreme cases being dilation and compaction bands (no slip). This transition is generally attributed to an increase in the mean stress, and our study is a further confirmation of this. While the effect of the Lode angle is less well documented, the experimental and theoretical results clearly show here that, at a given mean stress, the response is more brittle for high Lode angles and more ductile for low angles (state close to the axisymmetric compression state), this in quite noticeable proportions.

Journal : Large 11440 | Dispatch : 10-2-2023 | Pages : 14
Article No. : 1811 | ☐ LE | ☐ TYPESET
MS Code : AGEO-D-22-01165R1 | ☑ CP | ☑ DISK

5 Conclusion

In the scope of this study, an original three-invariant constitutive model was first presented for a well-studied Vosges sandstone. In the context of bifurcation theory, this general model was used to evaluate theoretical predictions of strain localization for unconventional loading paths, in the form of deformation bands. These predictions have been further evaluated in comparison with full-field experimental observations and alternative models.

The proposed yield surface, with both mean stress and Lode angle dependency, has been derived from a large number of mechanical loading experiments, including triaxial, biaxial and true triaxial invariant controlled loading paths. With the flexibility of a combined linear–exponential and van Eekelen function, the yield surface showed a good fit with experimental peak stresses over the wide range of axisymmetric and non-axisymmetric loading paths, in both the brittle and brittle–ductile transition regimes.

Using this model, a bifurcation analysis was conducted for a series of 10 laboratory loading tests in true triaxial conditions. For these experiments, local deformation measurements revealed a marked variation in the normals to the yield surface and direction of plastic strain at the peak stress, in both the octahedral (deviatoric) and meridian planes. This tendency results in a continuous evolution of the band kinematic predictions, where the orientation and dilatancy angles of the bands increase nonlinearly with an increase in the Lode angle and a decrease in the mean stress. This prediction is both consistent with the expected decrease in the ductility of the material and with full-field experimental measurements of the localized regions. It was also evidenced that the proposed non-associated three-invariant model performs better than simplified alternative models in predicting the band kinematics.

The findings presented herein demonstrate the validity and potential for this general bifurcation framework to corroborate observations in terms of the kinematics of so-called mature deformation bands, i.e., instigating a softening response, in porous rocks. The complementary role of early localization, i.e., emerging prior to the peak stress, and its relation to a later bifurcation state still needs to be investigated, perhaps from a different perspective.

Appendix 1: Elasto-plastic formulation

For an elasto-plastic material with additive incremental strain decomposition, $d\epsilon_{ij} = d\epsilon^e_{ij} + d\epsilon^p_{ij}$, the elastic and plastic strains are, respectively, defined as

$$d\epsilon^e_{ij} = C_{ijkl}\, d\sigma_{kl}\ ,\ d\epsilon^p_{ij} = d\lambda P_{ij}\ , \tag{17}$$

where $\mathbf{C}$ is the elastic compliance tensor and $\mathbf{P} = \frac{\partial G}{\partial \boldsymbol{\sigma}}$ is the direction of plastic strain. The magnitude of plastic deformation is determined by the plastic multiplier $d\lambda$, according to the flow rule. The incremental stress tensor, $d\sigma(d\epsilon)$, is therefore written as

$$d\sigma_{ij} = E_{ijkl}(d\epsilon_{kl} - d\lambda\, P_{kl})\ , \tag{18}$$

where $\mathbf{E}$ is the elastic stiffness tensor, *i.e.,* the inverse of $\mathbf{C}$. Considering isotropic hardening in the material, the consistency condition, $F = 0$ and $dF = 0$, is expressed in the form of

$$Q_{ij}\, d\sigma_{ij} - H d\lambda = 0\ , \tag{19}$$

where $\mathbf{Q} = \frac{\partial F}{\partial \boldsymbol{\sigma}}$ is the normal to the yield surface and H is a plastic coefficient. Combining Eqs. (18) and (19), the plastic multiplier can be written as

$$d\lambda = \frac{1}{h}\, Q_{uv}\, E_{uvrs}\, d\epsilon_{rs}\ , \tag{20}$$

with $h = H + Q_{ij}E_{ijkl}P_{kl}$.

This equation for the plastic multiplier is inserted back into the stress–strain relation in Eq. (18), resulting in

$$d\sigma_{ij} = E_{ijkl}(d\epsilon_{kl} - \frac{1}{h} Q_{uv}E_{uvrs}d\epsilon_{rs}P_{kl})\ . \tag{21}$$

Alternatively,

$$d\sigma_{ij} = L_{ijkl}\, d\epsilon_{kl}\ , \tag{22}$$

with the elasto-plastic constitutive tensor $\mathbf{L}$ as in Eq. (1).

Appendix 2: Invariants derivatives

The derivatives of the principal invariants (I_1,J_2,J_3) are first expressed as

$$\begin{aligned} \frac{\partial I_1}{\partial \sigma_{ij}} &= \delta_{ij}\ , \\ \frac{\partial J_2}{\partial \sigma_{ij}} &= s_{ij}\ , \\ \frac{\partial J_3}{\partial \sigma_{ij}} &= \delta_{pi}\delta_{jq}s_{qr}s_{rp} - \frac{1}{3}\delta_{pq}\delta_{ki}\delta_{jk}s_{qr}s_{rp}\ , \end{aligned} \tag{23}$$

where s_{ij} is the deviatoric part of the stress tensor resulting from its additive decomposition, $\sigma_{ij} = \frac{1}{3}\sigma_{kk}\delta_{ij} + s_{ij}$. Using these results, the derivatives of the octahedral-Lode invariants can therefore be written as

Journal : Large 11440 | Dispatch : 10-2-2023 | Pages : 14
Article No. : 1811 | LE | TYPESET
MS Code : AGEO-D-22-01165R1 | CP | DISK

$$\frac{\partial \sigma_m}{\partial \sigma_{ij}} = \frac{1}{3}\delta_{ij} \; ,$$
$$\frac{\partial \tau_{oct}}{\partial \sigma_{ij}} = \frac{s_{ij}}{3\tau_{oct}} \; ,$$
$$\frac{\partial \theta_\sigma}{\partial \sigma_{ij}} = \frac{-\sqrt{2}}{3\sin(3\theta_\sigma)\tau_{oct}^3} \left(s_{jr}s_{ri} - \delta_{ij}\tau_{oct}^2 - \frac{\sqrt{2}\cos(3\theta_\sigma)\tau_{oct}}{2} s_{ij} \right) . \tag{24}$$

Acknowledgements 3SR Lab. is part of the LabEx Tec 21 (Investissements d'Avenir - grant agreement n°ANR-11-LABX-0030).

Data availability The datasets generated during and/or analyzed during the current study are available from the corresponding author upon reasonable request.

References

1. Alexeev AD, Revva VN, Bachurin LL, Prokhorov IY (2008) The effect of stress state factor on fracture of sandstones under true triaxial loading. Int J Fract. https://doi.org/10.1007/s10704-008-9214-6
2. Aydin A, Johnson AM (1978) Development of faults as zones of deformation bands and as slip surfaces in sandstone. Pure Appl Geophys 116(4–5):931–942 (**Publisher: Springer**)
3. Bésuelle P (2021) Caractérisation du comportement anisotrope de l'argilite du Callovo-Oxfordien. Technical report, ANDRA, Grenoble
4. Bésuelle P (2001) Compacting and dilating shear bands in porous rock: theoretical and experimental conditions. J Geophys Res: Solid Earth 106(B7):13435–13442. https://doi.org/10.1029/2001JB900011
5. Bésuelle P, Rudnicki JW (2004) Localization: shear bands and compaction bands. In: Guéguen Y, Boutéca M (eds) Mechanics of fluid-saturated rocks, vol 89. International geophysics series. Elsevier academic press, Burlington, pp 219–321
6. Bésuelle P, Desrues J, Raynaud S (2000) Experimental characterisation of the localisation phenomenon inside a Vosges sandstone in a triaxial cell. Int J Rock Mech Min Sci 37(8):1223–1237. https://doi.org/10.1016/S1365-1609(00)00057-5
7. Bésuelle P, Baud P, Wong T-F (2003) Failure mode and spatial distribution of damage in Rothbach sandstone in the brittle-ductile transition. Pure Appl Geophys 160(5):851–868
8. Bigoni D, Piccolroaz A (2004) Yield criteria for quasibrittle and frictional materials. Int J Solid Struct 41(11):2855–2878. https://doi.org/10.1016/j.ijsolstr.2003.12.024
9. Chambon R, Crochepeyre S (1998) Daphnis: a new model for the description of post-localization behaviour: application to sands. Mech Cohes-Frict Mater 3(2):127–153. https://doi.org/10.1002/(SICI)1099-1484(199804)
10. Charalampidou E-M, Hall SA, Stanchits S, Lewis H, Viggiani G (2011) Characterization of shear and compaction bands in a porous sandstone deformed under triaxial compression. Tectonophysics 503(1–2):8–17. https://doi.org/10.1016/j.tecto.2010.09.032
11. Chemenda AI, Mas D (2016) Dependence of rock properties on the Lode angle: experimental data, constitutive model, and bifurcation analysis. J Mech Phys Solid 96:477–496. https://doi.org/10.1016/j.jmps.2016.08.004
12. Couture C (2020) Mechanical characterization of porous sandstones in true triaxial conditions: diffuse and localized deformation, effect of anisotropy. PhD thesis, Université Grenoble Alpes, Grenoble, France
13. Couture C, Bésuelle P (2022) A true triaxial experimental study on porous Vosges sandstone: from strain localization precursors to failure using full-field measurements. Int J Rock Mech Min Sci 153:105031. https://doi.org/10.1016/j.ijrmms.2021.105031
14. Darve F, Nicot F, Wautier A, Liu J (2021) Slip lines versus shear bands: two competing localization modes. Mech Res Commun 114:103603. https://doi.org/10.1016/j.mechrescom.2020.103603
15. Davatzes NC, Aydin A, Eichhubl P (2003) Overprinting faulting mechanisms during the development of multiple fault sets in sandstone, Chimney Rock fault array, Utah, USA. Tectonophysics 363(1–2):1–18. https://doi.org/10.1016/S0040-1951(02)00647-9
16. Descamps F, da Silva MR, Schroeder C, Verbrugge J-C, Tshibangu J (2012) Limiting envelopes of a dry porous limestone under true triaxial stress states. Int J Rock Mech Min Sci 56:88–99
17. Desrues J, Chambon R (2002) Shear band analysis and shear moduli calibration. Int J Solid Struct 39(13):3757–3776. https://doi.org/10.1016/S0020-7683(02)00177-4
18. Desrues J, Andò E, Mevoli FA, Debove L, Viggiani G (2018) How does strain localise in standard triaxial tests on sand: revisiting the mechanism 20 years on. Mech Res Commun 92:142–146. https://doi.org/10.1016/j.mechrescom.2018.08.007
19. Feng X-T, Zhang X, Kong R, Wang G (2016) A novel Mogi type true triaxial testing apparatus and its use to obtain complete stress-strain curves of hard rocks. Rock Mech Rock Eng 49:1649–1662. https://doi.org/10.1007/s00603-015-0875-y
20. Fossen H, Soliva R, Ballas G, Trzaskos B, Cavalcante C, Schultz RA (2018) A review of deformation bands in reservoir sandstones: geometries, mechanisms and distribution. Geol Soci 459(1):9–33. https://doi.org/10.1144/SP459.4
21. Gudehus G, Nübel K (2004) Evolution of shear bands in sand. Géotechnique 54(3):187–201. https://doi.org/10.1680/geot.2004.54.3.187
22. Haimson B, Chang C (2000) A new true triaxial cell for testing mechanical properties of rock, and its use to determine rock strength and deformability of Westerly granite. Int J Rock Mech Min Sci 37(1):285–296. https://doi.org/10.1016/S1365-1609(99)00106-9
23. Haimson B, Rudnicki JW (2010) The effect of the intermediate principal stress on fault formation and fault angle in siltstone. J Struct Geol 32(11):1701–1711. https://doi.org/10.1016/j.jsg.2009.08.017
24. Handin J, Heard HC, Magouirk JN (1967) Effects of the intermediate principal stress on the failure of limestone, dolomite, and glass at different temperatures and strain rates. J Geophys Res 72(2):611–640. https://doi.org/10.1029/JZ072i002p00611
25. Hill R (1962) Acceleration waves in solids. J Mech Phys Solids 10(1):1–16. https://doi.org/10.1016/0022-5096(62)90024-8
26. Ingraham M, Issen K, Holcomb D (2013) Response of Castlegate sandstone to true triaxial states of stress. J Geophys Res: Solid Earth 118(2):536–552. https://doi.org/10.1002/jgrb.50084
27. Issen KA, Challa V (2008) Influence of the intermediate principal stress on the strain localization mode in porous sandstone. J Geophys Res. https://doi.org/10.1029/2005JB004008
28. Issen KA, Rudnicki JW (2000) Conditions for compaction bands in porous rock. J Geophys Res: Solid Earth 105(B9):21529–21536. https://doi.org/10.1029/2000JB900185
29. Labuz JF, Dai S-T, Papamichos E (1996) Plane-strain compression of rock-like materials. Int J Rock Mech Min Sci Geomech

Journal : Large 11440 Dispatch : 10-2-2023 Pages : 14
Article No. : 1811 ☐ LE ☐ TYPESET
MS Code : AGEO-D-22-01165R1 ☑ CP ☑ DISK

Abstr 33(6):573–584. https://doi.org/10.1016/0148-9062(96)00012-5
30. Lade PV, Duncan JM (1975) Elastoplastic stress-strain theory for cohesionless soil. J Geotechn Geoenviron Eng,
31. Lade PV (1977) Elasto-plastic stress-strain theory for cohesionless soil with curved yield surfaces. Int J Solid Struct 13(11):1019–1035. https://doi.org/10.1016/0020-7683(77)90073-7
32. Lanata P (2015) Full-field experimental characterization of mechanical behaviour and failure in a porous rock in plane strain compression: homogeneous deformation and strain localization. PhD thesis, Univ. Grenoble, France
33. Le Bouil A, Amon A, Sangleboeuf J-C, Orain H, Bésuelle P, Viggiani G, Chasle P, Crassous J (2014) A biaxial apparatus for the study of heterogeneous and intermittent strains in granular materials. Granular Matt 16:1–8. https://doi.org/10.1007/s10035-013-0477-x
34. Loret B (1992) Does deviation from deviatoric associativity lead to the onset of flutter instability? J Mech Phys Solids 40(6):1363–1375. https://doi.org/10.1016/0022-5096(92)90019-X
35. Ma X, Haimson BC (2016) Failure characteristics of two porous sandstones subjected to true triaxial stresses. J Geophys Res: Solid Earth 121(9):6477–6498. https://doi.org/10.1002/2016JB012979
36. Ma X, Rudnicki JW, Haimson BC (2017) Failure characteristics of two porous sandstones subjected to true triaxial stresses: applied through a novel loading path. J Geophys Res: Solid Earth 122(4):2525–2540. https://doi.org/10.1002/2016JB013637
37. Mandel J (1966) Conditions de stabilité et postulat de Drucker. In: Rheology and Soil Mechanics/Rhéologie et Mécanique des Sols. Springer, Berlin & Heidelberg, pp. 58–68
38. Maso J-C, Lerau J (1980) Mechanical behaviour of Darney sandstone (Vosges, France) in biaxial compression. Int J Rock Mech Min Sci Geomech Abstr 17(2):109–115. https://doi.org/10.1016/0148-9062(80)90262-4
39. Matsuoka H, Nakai T (1974) Stress-deformation and strength characteristics of soil under three different principal stresses. Proceed Japan Soci Civil Eng 1974(232):59–70. https://doi.org/10.2208/jscej1969.1974.232_59
40. Michelis P (1987) True triaxial cyclic behavior of concrete and rock in compression. Int J Plast 3(3):249–270. https://doi.org/10.1016/0749-6419(87)90022-2
41. Millien A (1993) Comportement anisotrope du grès des Vosges : élasto-plasticité, localisation, rupture. PhD thesis, Université Joseph-Fourier - Grenoble I
42. Mogi K (2007) Experimental rock mechanics. Taylor & Francis, London, https://doi.org/10.1201/9780203964446
43. Molenkamp F (1985) Comparison of frictional material models with respect to shear band initiation. Géotechnique 35(2):127–143. https://doi.org/10.1680/geot.1985.35.2.127
44. Mourlas C, Pardoen B, Bésuelle P Large-scale failure prediction of clay-rock from small scale damage mechanisms of the rock medium using multiscale modelling. Int J Rock Mech Min Sci (accepted)
45. Olsson WA (1999) Theoretical and experimental investigation of compaction bands in porous rock. J Geophys Res 104(B4):7219–7228. https://doi.org/10.1029/1998JB900120
46. Ord A, Vardoulakis I, Kajewski R (1991) Shear band formation in Gosford sandstone. Int J Rock Mech Min Sci Geomech Abstr 28(5):397–409. https://doi.org/10.1016/0148-9062(91)90078-Z
47. Ord A, Vardoulakis I, Kajewski R (1991) Shear band formation in Gosford sandstone. Int J Rock Mech Min Sci Geomech Abstr 28(5):397–409
48. Paterson MS, Wong TF (2005) Experimental rock deformation - The Brittle Field. Springer, Berlin https://doi.org/10.1007/b137431
49. Poorooshasb HB, Holubec I, Sherbourne AN (1966) Yielding and flow of sand in triaxial compression: part i. Can Geotech J 3(4):179–190. https://doi.org/10.1139/t66-023
50. Rice JR (1976) The localization of plastic deformation. In: Koiter, W.T. (ed.) Theoretical and applied mechanics, North-Holland Pub. Comp., Delft. Proc. 14th Int. Cong. Theor. Appl. Mech, pp. 207–220
51. Rudnicki JW, Rice J (1975) Conditions for the localization of deformation in pressure-sensitive dilatant materials. J Mech Phys Solid 23(6):371–394. https://doi.org/10.1016/0022-5096(75)90001-0
52. Sriapai T, Walsri C, Fuenkajorn K (2013) True-triaxial compressive strength of Maha Sarakham salt. Int J Rock Mech Min Sci 61:256–265. https://doi.org/10.1016/j.ijrmms.2013.03.010
53. Sulem J, Ouffroukh H (2006) Shear banding in drained and undrained triaxial tests on a saturated sandstone: porosity and permeability evolution. Int J Rock Mech Min Sci 43(2):292–310. https://doi.org/10.1016/j.ijrmms.2005.07.001
54. Sulem J, Vardoulakis I, Papamichos E, Oulahna A, Tronvoll J (1999) Elasto-plastic modelling of Red Wildmoor sandstone. Mech Cohes-Frict Mater 4(3):215–245. https://doi.org/10.1002/(SICI)099-1484(199905)
55. Takahashi M, Koide H (1989) Effect of the intermediate principal stress on strength and deformation behavior of sedimentary rocks at the depth shallower than 2000 m. In: Maury V, Fourmaintraux D (eds) Int Symp Rock Great Depth. Balkema, Pau, France, pp 19–26
56. Thomas TY (1958) Plastic flow and fracture in solids. J Math Mech 7(3):291–322
57. Van Eekelen HAM (1980) Isotropic yield surfaces in three dimensions for use in soil mechanics. Int J Numer Anal Meth Geomech 4(1):89–101. https://doi.org/10.1002/nag.1610040107
58. Vardoulakis IG, Sulem J (2004) Bifurcation analysis in geomechanics. CRC Press, London, https://doi.org/10.1201/9781482269383
59. Wong T-F, Baud P (2012) The brittle-ductile transition in porous rock: a review. J Struct Geol 44:25–53. https://doi.org/10.1016/j.jsg.2012.07.010
60. Wu S, Zhang S, Guo C, Xiong L (2017) A generalized nonlinear failure criterion for frictional materials. Acta Geotechnica 12:1353–1371. https://doi.org/10.1007/s11440-017-0532-6
61. Yong RN, McKyes E (1971) Yield and failure of a clay under triaxial stresses. J Soil Mech Found Div 97(1):159–176

Journal : Large 11440 Dispatch : 10-2-2023 Pages : 14
Article No. : 1811 ☐ LE ☐ TYPESET
MS Code : AGEO-D-22-01165R1 ☑ CP ☑ DISK

Journal : **11440**
Article : **1811**

Author Query Form

Please ensure you fill out your response to the queries raised below and return this form along with your corrections

Dear Author

During the process of typesetting your article, the following queries have arisen. Please check your typeset proof carefully against the queries listed below and mark the necessary changes either directly on the proof/online grid or in the 'Author's response' area provided below

Query	Details Required	Author's Response
AQ1	Kindly check and confirm that the affiliation details have been correctly present.	
AQ2	Kindly check and provide complete details for the references [30, 44] in the list.	
AQ3	Kindly check and confirm that the appendix part equations have been sequencially rearranged along with text part equations.	